Monthly Notices of the ROYAL ASTRONOMICAL SOCIETY

MNRAS **522,** 1451–1463 (2023)
Advance Access publication 2023 April 17

https://doi.org/10.1093/mnras/stad1081

Fuzzy Aquarius: evolution of a Milky-way like system in the Fuzzy Dark Matter scenario

Matteo Nori [1,2]★ Andrea V. Macciò [1,2,3] and Marco Baldi [4,5,6]

[1]*New York University Abu Dhabi, PO Box 129188 Saadiyat Island, Abu Dhabi, United Arab Emirates*
[2]*Center for Astro, Particle and Planetary Physics (CAP3), New York University Abu Dhabi, PO Box 129188 Saadiyat Island, Abu Dhabi, United Arab Emirates*
[3]*Max Planck Institut für Astronomie, Königstuhl 17, D-69117 Heidelberg, Germany*
[4]*Dipartimento di Fisica e Astronomia, Alma Mater Studiorum - University of Bologna, Via Piero Gobetti 93/2, I-40129 Bologna BO, Italy*
[5]*INAF - Osservatorio Astronomico di Bologna, Via Piero Gobetti 93/3, I-40129 Bologna BO, Italy*
[6]*INFN - Istituto Nazionale di Fisica Nucleare, Sezione di Bologna, Viale Berti Pichat 6/2, I-40127 Bologna BO, Italy*

Accepted 2023 April 4. Received 2023 April 3; in original form 2022 October 14

ABSTRACT

We present the first high-resolution zoom-in simulation of a Milky-way-like halo extracted from the Aquarius Project in the Fuzzy Dark Matter (FDM) framework. We use the *N*-body code AX-GADGET, based on a particle-oriented solution of the Schrödinger–Poisson equations, able to detail the complexity of structure formation while keeping track of the quantum effects in FDM. The halo shows a cored density profile, with a core size of several kpc for an FDM mass of $m_\chi = 2.5h \times 10^{-22}$ eV/c^2. A flattening is observed also in the velocity profile, representing a distinct feature of FDM dynamics. We provide a quantitative analysis of the impact of *fuzziness* on subhaloes in terms of abundance, mass, distance, and velocity distribution functions, and their evolution with redshift. Very interestingly, we show that all collapsed structures, despite showing a flat density profile at $z = 0$, do not reach the *solitonic* ground state at the time of formation: on the contrary, they asymptotically converge to it on a time-scale that depends on their mass and formation history. This implies that current limits on FDM mass – obtained by applying simple scaling relations to observed galaxies – should be taken with extreme care, since single objects can significantly deviate from the expected asymptotic behaviour during their evolution.

Key words: (cosmology:) dark matter – methods: numerical.

1 INTRODUCTION

Among the many unanswered questions about the fundamental processes governing the evolution of our Universe, the ones regarding the elusive nature of dark matter are some of the most puzzling. Its extremely weak interaction (or a lack thereof) with standard matter and its low intrinsic velocity are the two main properties of the standard Cold Dark Matter (CDM) cosmological model, both necessary to avoid unobserved electromagnetic dark matter signals and to be consistent with the formation of large-scale structures. These properties, however, can be associated with several physical entities or reproduced by several processes.

In fact, many possible sources have been historically investigated – with different success – as possible candidates for dark matter (see e.g. Bertone, Hooper & Silk 2005), such as astrophysical objects (e.g. like Massive Compact Halo Objects (MACHOs) Alcock et al. 1993), physical effective mechanisms (e.g. like Modified Newtonian dynamics (MOND) Milgrom 1983), as well as new fundamental particles beyond the standard model of particle physics, like Weakly Interactive Massive Particles (WIMPs; Jungman, Kamionkowski & Griest 1996).

The WIMP model, in particular, was regarded as the most promising model of dark matter for many years, due to the following peculiar coincidence: assuming the interaction between dark and standard matter to be weak enough to avoid electromagnetic detection but strong enough to ensure thermal equilibrium in the early universe before the eventual decoupling of the dark component, the mass of such dark matter particle would fall in the 100–1000 GeV/c^2 range, which is coincidentally similar to the range associated with a weak force (see e.g. Kamionkowski 1998).

With the advent of new cosmological surveys of the Cosmic Microwave Background like Wilkinson Microwave Anisotropy Probe (WMAP, Bennett et al. 2013) and Planck (Planck Collaboration XIII 2016), the WIMP particle-based model was still considered as one of the front-runner models for dark matter. Nevertheless, the lack of a detection in this mass range after many years of continuous search by dedicated particle accelerator experiments like the Large Hadron Collider (LHC, see e.g. Albert et al. 2017; Danninger 2017; Buonaura 2018) has been eroding the consensus surrounding WIMPs, in favour of other particles in mass ranges previously unexplored.

Among these, an interesting dark matter candidate could be linked to the axion particle (see again Kamionkowski 1998), arising from the CP-symmetry breaking in quantum chromodynamics (QCD) (Peccei & Quinn 1977a,b). From the QCD axion – which is tightly related to the strong CP problem – a more general concept of a pseudo-scalar bosonic particle can be derived to encompass a much broader class of axion-like particles (ALPs). Within this category spanning over an astonishingly wide range of masses of the order 10^{-24}–10^{0} eV/c^2, there are particles that can be regarded as well-

★ E-mail: matteo.nori@nyu.edu

motivated dark matter candidates well below the WIMP mass scale (see Ferreira 2021, for a recent and comprehensive review on the subject).

The general ALP dynamics is characterized by a wave-like quantum self-interaction that is mainly set by its mass. The latter is, in fact, related both to the timing of the dynamical regimes ALPs exhibit with respect to the background cosmic dynamics as well as to the the strength of the self-interaction and its consequences for structure formation. In particular, the ALP mass sets the cosmological epoch at which the associated dark matter component exits from the oscillatory regime – which is a peculiar feature of the axion potential – and begins to cluster, thus affecting in different ways the evolution of large-scale structures when ALP role as a dark matter candidate is considered (see e.g. Sikivie 2008).

A crucial distinction concerning the relative timing of the end of the oscillatory regime with respect to the time of matter–radiation equality can be then drawn for ALPs with mass above or below $10^{-10}\mathrm{eV}/c^2$. Above this value, dark matter begins to cluster before equality, thus effectively segregating a large fraction of the total dark matter content in gravitationally bound *axion miniclusters* by the time of baryon decoupling from radiation (see e.g. the early works of Kolb & Tkachev 1993, 1994). On the contrary, for lower values of the mass, the density distribution of the ALP field at matter–radiation equality can be essentially described by adding a small-scale correction to the usual CDM density distribution related to its self-interaction (Hu, Barkana & Gruzinov 2000).

The clustering process differs in the ALP dark matter and CDM models, as the typical wave-like dynamics of the ALP acts as an effective net repulsive force below a certain scale, thus admitting a non-degenerate self-gravitating stable solution – called *soliton* – whose properties scale with the ALP mass (see e.g. Marsh 2016). In recent years, a wide range of experiments have been designed to detect QCD axions or ALPs and to investigate their possible link to dark matter (see e.g. Banerjee et al. 2020, for a recent overview): these include, e.g. resonant cavity experiments at various frequencies (McAllister et al. 2017, ORGAN; ADMX, Braine et al. 2020), dielectric haloscopes (MADMAX, Majorovits et al. 2020), detection-induced magnetic flux oscillations (ABRACADABRA, Ouellet et al. 2019), and NMR-based techniques (CASPEr, Graham & Rajendran 2013; ARIADNE, Arvanitaki & Geraci 2014).

In this work, we focus on the lower end of the ALP mass spectrum – in the range of 10^{-24}–$10^{-19}\mathrm{eV}/c^2$ – whose associated dark matter models are often referred to as Fuzzy Dark Matter (FDM). Masses in this range are often conveniently expressed in units of m_{22}, where $m_{22} \equiv 10^{-22}\mathrm{eV}/c^2$. As previously mentioned, the wave-like interaction of FDM acts as a net repulsive force and thus power is erased with respect to the fiducial CDM matter power spectrum at matter–radiation equality, effectively smoothing out density perturbations at small scales and thus leading to fewer collapsed structures at lower redshifts (Hu et al. 2000). Moreover, the particle mass is so light that the associated de Broglie wavelength and – as a direct consequence – the self-gravitating objects that can be formed are comparable with the galactic scales (see again Hu et al. 2000). These features are of particular cosmological interest, since FDM could be simultaneously involved in the development of a constant-density core in the innermost region of dark matter profiles – originally related to the cusp–core differentiation of Oh et al. (2011), which can be solved only in some mass ranges by the presence of baryons (see e.g. Tollet et al. 2016) – and the suppression of the typical CDM overabundance of galactic satellites (Klypin et al. 1999).

Numerical simulations of structure formation within FDM models have been initially performed by means of highly numerically intensive Adaptive Mesh Refinement (AMR) algorithms able to solve the Schrödinger–Poisson (SP) equations over a grid (see e.g. Schive, Tsai & Chiueh 2010; Mocz et al. 2017; Schive et al. 2018), leading to impressive and very detailed results on the properties of individual FDM-collapsed objects (see e.g. Woo & Chiueh 2009; Schive, Chiueh & Broadhurst 2014; Veltmaat, Niemeyer & Schwabe 2018). However, the computational cost of such an approach hindered the possibility to extend the investigation of late-time structure formation to large cosmological volumes. To address this issue, *N*-body codes were developed, initially only including the (linear) suppression in the initial conditions but neglecting the integrated effect of the FDM interaction during the subsequent dynamical evolution (see e.g. Schive et al. 2016; Armengaud et al. 2017; Iršič et al. 2017) – i.e. basically treating FDM as standard dark matter with a suppressed primordial power spectrum, similarly to what is routinely done in Warm Dark Matter (WDM) simulations (Bode, Ostriker & Turok 2001; Schneider et al. 2012).

In this manuscript, we present a high-resolution Milky-way-like dark matter system simulated in the FDM scenario; in particular, the system consists of a zoom-in simulations taken from the Aquarius project (Springel et al. 2008) (halo A – resolution level 3). The Aquarius project has been a cornerstone in understanding the relationship between halo and subhaloe properties, and it has been used as a benchmark for investigating other dark matter models beyond CDM in the past (as, e.g. WDM; Lovell et al. 2014). The main goal of this work is the analysis of the system properties and FDM specific observables and their evolution in time as resulting from the complex non-linear structure formation process in an FDM cosmology.

The zoom-in approach consists of a rationalized distribution of resolution elements within the simulation box, which allows to detail a region of interest – normally, a collapsed structure – with high resolution, while efficiently keeping track of its environment (see e.g. Katz et al. 1994; Navarro & White 1994). In this sense, zoom-in simulations represent an intermediate step bridging single-object simulations and bigger fixed-resolution cosmological simulations. By adopting this method, it is then possible to retain information about the cosmological context while reaching a higher resolution than a homogeneously represented *N*-body simulation.

The paper is organized as follows: in Section 2, we present the theoretical background related to FDM models; in Section 3, we detail the numerical aspects of this work, related to the simulation and the data production; in Section 4, we then present the main results of this work, regarding the halo and subhaloes; finally, in Section 5, we summarize our findings, discuss them, and draw our conclusions.

2 THEORY

In this section, we collect the fundamental equations that govern FDM dynamics. We here detail also the specific properties and scaling relations that are relevant to this work and that characterize FDM-collapsed structures.

2.1 FDM models

In FDM models, the mass of the dark matter particle is so tiny that the associated De-Broglie wavelength is of astrophysical scales, requiring the dynamical treatment of dark matter to take into account quantum interactions. FDM is thus usually described through a quantum bosonic field $\hat{\phi}$, under the assumption of condensation (Hu et al. 2000, 2017).

The Gross–Pitaevskii–Poisson equation describing the evolution of a massive bosonic field $\hat{\phi}$ reads (Gross 1961; Pitaevskii 1961)

$$i\frac{\hbar}{m_\chi}\,\partial_t\hat{\phi} = -\frac{\hbar^2}{m_\chi^2}\nabla^2\hat{\phi} + \Phi\hat{\phi}, \tag{1}$$

where m_χ represents the typical mass of the FDM particle and Φ is the Newtonian gravitational potential, which satisfies the standard Poisson equation

$$\nabla^2\Phi = 4\pi G\rho_b\,\delta/a, \tag{2}$$

where $\delta = (\rho - \rho_b)/\rho_b$ is the comoving density contrast with respect to the comoving background density ρ_b (Peebles 1980). Together, equations (1) and (2) form the so-called Schrödinger–Poisson (SP) system.

The system can be recast from a *field* description into a mathematically equivalent *fluid* one – associating the field amplitude and phase with fluid density ρ and a fluid velocity $\boldsymbol{v}$, respectively – with the use of the Madelung transformation (Madelung 1927)

$$\rho = |\hat{\phi}|^2 \tag{3}$$

$$\mathbf{v} = \frac{\hbar}{m_\chi}\Im\frac{\nabla\hat{\phi}}{\hat{\phi}}. \tag{4}$$

In the frame of an expanding universe – with a and $H = \dot{a}/a$ being the usual cosmological scale factor and Hubble function, respectively – we refer to $\mathbf{x}$ as the comoving distance and to the velocity $\mathbf{u}$ as the comoving equivalent of $\mathbf{v}$. The real and imaginary parts of equation (1) then translate into a continuity equation

$$\dot{\rho} + 3H\rho + \nabla\cdot(\rho\mathbf{u}) = 0 \tag{5}$$

and a modified Euler equation

$$\dot{\mathbf{u}} + 2H\mathbf{u} + (\mathbf{u}\cdot\nabla)\,\mathbf{u} = -\frac{\nabla\Phi}{a^2} + \frac{\nabla Q}{a^4}, \tag{6}$$

where an additional potential Q – accounting for the wave-like behaviour of the field – appears alongside the usual gravitational potential Φ.

The so-called Quantum Potential Q (QP hereafter) has the form

$$Q = \frac{\hbar^2}{2m_\chi^2}\frac{\nabla^2\sqrt{\rho}}{\sqrt{\rho}} = \frac{\hbar^2}{2m_\chi^2}\left(\frac{\nabla^2\rho}{2\rho} - \frac{|\nabla\rho|^2}{4\rho^2}\right) \tag{7}$$

and accounts for the purely quantum behaviour of the field (Bohm 1952). It is interesting to remark that, from a theoretical point of view, the quantum nature of dark matter that sources the QP is present in the usual Euler equation used to describe CDM as well: however, it is just safely negligible in the classical limit, as the factor $\hbar^2/m_\chi^2$ is extremely small for the typical eV–GeV mass ranges that has been historically considered for the CDM particle (see e.g. Bertone et al. 2005; Feng 2010).

2.2 FDM: scaling relations

The modified Euler–Poisson (mEP) system composed by equations (5), (6), and (2) that governs self-gravitating FDM dynamics

$$\begin{cases} \dot{\rho} + 3H\rho + \nabla\cdot(\rho\mathbf{u}) = 0 \\ \dot{\mathbf{u}} + 2H\mathbf{u} + (\mathbf{u}\cdot\nabla)\,\mathbf{u} = -\dfrac{\nabla\Phi}{a^2} + \dfrac{\nabla Q}{a^4} \\ \nabla^2\Phi = 4\pi G\rho_b\,\delta/a \end{cases} \tag{8}$$

is the fluid-equivalent of the SP system. It admits a spherically symmetric time-independent one-parameter family of solutions $\rho_{\rm sol}(r)$ that has no analytical form. The ground-state solution is usually referred to as the *solitonic* core, as its density profile saturates to a constant value in the centre. Despite the lack of an analytical form, it can be well approximated (see e.g. Schive et al. 2014) by

$$\rho_{\rm sol}(r,\,\rho_c,\,R_c) = \rho_c\left[1 + \alpha\left(\frac{r}{R_c}\right)^2\right]^{-8}, \tag{9}$$

where ρ_c is the core density and

$$R_c : \rho_{\rm sol}(r = R_c) = \rho_c/2 \tag{10}$$

is the half-density comoving radius, simply referred to as core radius, which is set by construction choosing the constant $\alpha = \sqrt[8]{2} - 1$.

The mEP system of equation (8) is invariant under the coordinate transformation via a generic constant λ (Ji & Sin 1994)

$$\begin{aligned}&\{\mathbf{x},\,t,\,\mathbf{u},\,\rho,\,M,\,\Phi,\,E\}\\ &\quad\to\left\{\lambda\tilde{\mathbf{x}},\,\lambda^2\tilde{t},\,\lambda^{-1}\tilde{\mathbf{u}},\,\lambda^{-4}\tilde{\rho},\,\lambda^{-1}\tilde{M},\,\lambda^{-2}\tilde{\Phi},\,\lambda^{-3}\tilde{E}\right\},\end{aligned} \tag{11}$$

where we also included the mass M and the energy E of the system.

It is possible to see that such transformation sets some scaling relations, in particular, the core density ρ_c, its radius R_c, and its mass M_c are thus linked through

$$R_c \propto \left(a\,m_\chi^2\,\rho_c\right)^{-1/4} \tag{12}$$

thanks to the intrinsically symmetric nature of the system (see e.g. Chavanis 2011; Chavanis & Delfini 2011, for a thorough analytical and numerical study).

In this work, we specifically use the term FDM cores to describe the one-parameter discreet family of spherically symmetric solutions – each associated with a different energy level – that satisfy the scaling relation $R_c \sim (a\rho_c)^{-1/4}$, with the *solitonic* core representing the densest ground-state solution (see e.g. Appendix B in Hui et al. 2017).

In a cosmological context, the linear density perturbation δ_k in Fourier space satisfies

$$\ddot{\delta}_k + 2H\dot{\delta}_k + \left(\frac{\hbar^2k^4}{4m_\chi^2a^4} - 4\pi G\rho_b\right)\delta_k = 0 \tag{13}$$

that directly sets the typical scale

$$k_Q(a) = \left(\frac{16\pi G\rho_b m_\chi^2}{\hbar^2}\right)^{1/4} a^{1/4} \tag{14}$$

for which the gravitational pull is balanced by the QP repulsion, sometimes referred as *quantum Jeans scale* in analogy with the homonym classical one (Chavanis 2012). This scale decreases as the Universe evolves, effectively shifting the scale of balance between quantum repulsion and gravitational attraction towards smaller and smaller values. As a result, dark matter structures that are able to collapse are thus characterized by a central core in the density profile, as the quantum interaction is able to sustain it against gravitational collapse even at lower redshifts, while a typical Navarro–Frenk–White (NFW) density profile is recovered at larger distances, where the contribution of quantum interaction is negligible compared to the gravitational one.

The scaling relation of equation (12) was first explicitly investigated in an astrophysical scenario with dedicated numerical simulations by Schive et al. (2014), where it was confirmed to hold for a sample of haloes at different redshifts in the mass range $10^9-10^{11}\,{\rm M}_\odot/{\rm h}$, simulated by directly solving the Schrödinger equation on a three-dimensional grid.

Many following works by different groups using a grid-based approach (see e.g. Schwabe, Niemeyer & Engels 2016; Du et al.

2017; Mocz et al. 2017; May & Springel 2021; Chan et al. 2022) confirmed the statistical validity of the relation for individual systems. The scaling relation was found to be generally valid also in *N*-body simulations (Nori & Baldi 2020), although a statistically higher normalization constant with respect to other works was observed, due to a possible correlation between the normalization and the dynamical state and/or mass of the specific system.

3 NUMERICAL METHODS

In this section, we introduce and describe the simulations presented in this work and the numerical algorithms used in the simulation process.

3.1 Zoom-in simulations and IC set-up

The results discussed in the present work are extracted from two simulations of the same individual system. In particular, we will systematically compare the main results of one of the haloes of the Aquarius Project (Springel et al. 2008, halo Aq-A-3) – simulated within the CDM scenario – with the one obtained from its re-simulated counterpart in the FDM context.

The two simulations are *zoom-in* simulations, meaning that their initial conditions are based on a rationalized distribution of resolution elements – particles, in the case of *N*-body codes – belonging to a collapsed object extracted from a parent low-resolution cosmological simulations.

In terms of initial conditions, the distribution of initial density perturbations have been modified accordingly to the FDM case. The typical suppression of the initial power spectrum induced by FDM was taken into account by providing a suitable initial power spectrum for the desired FDM cosmology. To calculate the cosmological initial power-spectrum at the initial redshift, we used axionCAMB (Hlozek et al. 2015), assuming the totality of matter to be fuzzy with a boson mass of $m_{22} = 2.5\ h$. Such a low value for m_{22} is chosen to amplify the effects on a MW-like system and it represents a proof of concept, as it is ruled out by current constraints on FDM mass (e.g. from Lyman-α forest constraints; Nori et al. 2019).

The suppression of the initial power spectrum in the FDM case can be visualized in Fig. 1, where the transfer functions $T(k) = \sqrt{P(k)/P_{CDM}(k)}$ ratios are plotted at the initial redshift $z = 127$. For the interested readers, we included the transfer function of a WDM model that has the same *half-mode* wave number $k_{\rm hm}$ – defined as the value of k for which $T(k_{\rm hm}) = 0.5$ – corresponding to a WDM mass of $m_{\rm WDM} \sim 0.84$ keV/c^2 (we used equations 5–6 in Viel et al. 2005). It is worth noting, however, that a similar suppression in the initial power spectrum should not be hastily used to draw comparisons between WDM and FDM models, especially in the properties of structures at low redshift. In fact, FDM features an intrinsically different dynamic (i.e. the additional non-linear quantum interaction) with respect to WDM, whose integrated effects should be cautiously taken into account. The remaining simulation technical details of the CDM and FDM simulations are consistent, as originating from the same set-up. In particular, the high resolution region is characterized by a gravitational softening of $\epsilon \sim 120$ pc and $M_p \sim 5 \times 10^4 M_\odot$ particle mass (see Springel et al. 2008, Table 1, Aq-A-3).

In terms of dynamical evolution, the two simulations effectively share the same background cosmology with the only exception being the dark matter dynamics. The original halo from Springel et al. (2008) was simulated using P-GADGET3 and its FDM counterpart has been simulated with a modified version of P-GADGET3 that include FDM phenomenology called AX-GADGET (Nori & Baldi 2018). The modified code makes use of the P-GADGET3 Smoothed Particle Hydrodynamics (SPH) routines to solve FDM dynamics in the Madelung framework; interested readers can find more information on the code in Nori & Baldi (2018) (as well as in Nori et al. 2019; Nori & Baldi 2020).

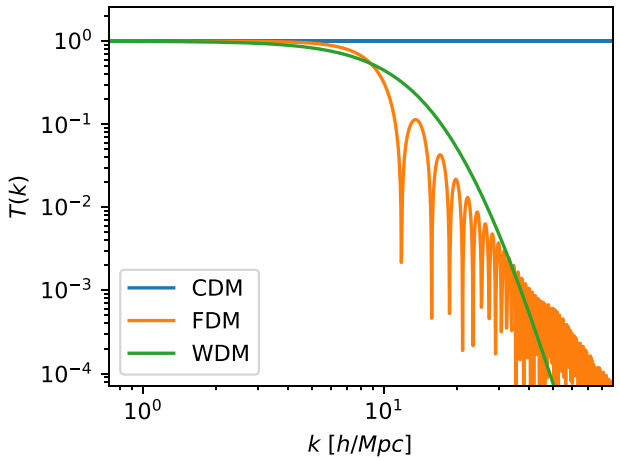

Figure 1. Transfer function of the initial power spectrum, in the FDM ($m_{22} = 2.5h$) and CDM case. A WDM model with the same half-mass mode $k_{\rm hm}$ as FDM, corresponding to $m_{\rm WDM} = 0.84$ keV/c^2, is displayed for the interested readers.

The differences observed in the final properties between the two simulations are then to be considered as consequences of the two main aspects that differentiate FDM from CDM phenomenology; on the one hand, the smoother density distribution of the early FDM universe at small scales, encoded in the simulations as a suppression of the initial FDM power spectrum, on the other hand, the additional QP term in the equations of motion of dark matter.

As a final note, we report the cosmological background parameters used in the FDM simulation as well as in the original CDM one from Springel et al. (2008): $\Omega_m = 0.25$, $\Omega_\Lambda = 0.75$, $H_0 = 73$ km/s/Mpc together with the initial power-spectrum parameters $n_s = 1$ and $\sigma_8 = 0.9$.

3.2 Halo identification, merger tree construction, and fragmentation correction

To identify collapsed objects and build the merger tree, we use the same methods (based on the SUBFIND code) as in Springel et al. (2008). The SUBFIND code relies on a Friends-of-friends algorithm (Davis et al. 1985) tailored to identify halo systems, which are then subdivided and disentangled in subhaloes based on binding energy criteria. On a technical level, we impose a minimum number of 64 particles for subhaloes to be included in the analysis.

In the following, we will refer to the overall dark matter system centred in the potential minimum as the halo, while we refer to the substructures within the halo as subhaloes.

The information related to the evolution of structures is encoded by the merger tree, reconstructed from the several snapshots of the simulation taken at different redshifts. Making use of the constant and unique numerical identifier of each particle in the simulation, it is possible to track the evolution of particles ensembles, associating progenitors, and descendants (i.e. haloes that share a large number of particles at different redshifts), and identify merger events where multiple haloes coalesce into one. By comparing each snapshot with

the previous one, it is also possible to quantify at a given snapshot the share of mass of an object that has been accreted via merger with other objects, quantity that we define as $M_{\rm merged}$.

It is important to know that not all the collapsed objects that are present in the FDM simulations can be safely taken in consideration. In fact, a known problem that affects *N*-body simulations with suppressed initial condition at small scales is the so-called *numerical fragmentation* problem (Wang & White 2007, and references therein), which indicates the formation of small collapsed objects that have numerical origin and do not arise from the gravitational evolution of primordial physical overdensities.

To filter subhaloes from this spurious contamination, we use the same approach based on cuts in number of particles, mass, and shape used in Nori et al. (2019) (and based in turn on Wang & White 2007; Lovell et al. 2014). In practice, this requires to impose a cut-off in mass, the number of particles, and the shape on FDM subhaloes; these cuts are a conservative way to safely regard the remaining sample as physically meaningful.

The empirical estimate for the mass cut-off scales with the dimensionless power spectrum peak scale k_{peak} and the interparticle distance d (Wang & White 2007; Lovell et al. 2014) as

$$M_{CUT} \sim 5\ \rho_b\ d\ /\ k_{peak}^2 \tag{15}$$

above which it is possible to say that most of the haloes have a physical origin. In the case of our FDM simulation, this value is approximately $M_{CUT} \sim 5 \times 10^8 {\rm M}_\odot/{\rm h}$ representing $\sim 10^4$ particles (a factor 10 higher than the cut-ff in the number of particles suggested by Lovell et al. (2014)). As for the shape, the halo particles are traced back to their original position in the initial conditions and the ratio of the minor and major semi-axes – obtained by computing the inertia tensor of the equivalent triaxial ellipsoid and defined as *sphericity* s – is used as a constraint. A cut-off is imposed to s in the initial condition, below which the haloes are considered spurious; in this work, we use the value $s_{CUT} = 0.16$ of Lovell et al. (2014) that we verified being valid also in the FDM case in Nori et al. (2019).

4 RESULTS

In this section, we present the results obtained from the Aquarius FDM zoom-in simulation and we compare it with its CDM counterpart. In the comparison between the two, we highlight the specific effects introduced by the different dark matter behaviour. In particular, we first detail the global properties of subhaloes, their cumulative distributions in terms of mass, position, and velocity in FDM and CDM cosmologies. We then focus on the specific FDM properties of the halo and subhalo cores to characterize the evolution of their features.

4.1 FDM versus CDM comparison of global properties

As a first visual comparison, in Fig. 2 we present two density maps at $z = 0$ of the CDM (left panels) and FDM (right panels) high-resolution region of 3.5 kpc/h per side (top panels) and a zoom of 0.7 kpc/h per side on the main system (bottom panels). The difference between the two scenarios in terms of number of structures is striking, especially for the large number of small structures that characterize CDM and are not present in FDM. To highlight this feature in a three-dimensional space, a density rendering is displayed in Fig. 3. The images depict the main halo at $z = 0$ for the CDM (left) and FDM (right) simulations, within a box of 0.7 kpc/h side, using the same iso-density contour level. For the interested readers, a 360° rotating version of Fig. 3 can be found in the online materials.

The following detailed statistical analyses on the properties of subhaloes take into account the effect of the numerical fragmentation in the FDM simulation. In fact, not all the FDM systems represent a physical collapsed object as they may be the artificial result of numerical noise in the initial conditions, as discussed in Section 3.2. Depending on the situation, we will include a comparison with the subsample of CDM subhaloes that satisfies the same requirement $M_{sat} > M_{CUT}$ (referred as CDM-CUT) to specifically compare FDM and CDM results in the same mass range. In our analysis, we include all SUBFIND structures – isolated haloes and subhaloes – whose distance is less than 400 kpc/h from the halo centre, which is approximately ∼1.5 times the virial radius in the CDM case. For the remainder of this paper, we refer to all of these structures as subhaloes for brevity.

4.1.1 *Number and mass of subhaloes*

As visually clear from Fig. 2, the Milky-way like system under consideration presents significant differences in the number of subhaloes when comparing the FDM and CDM frameworks.

First of all, let us consider the number of subhaloes and the mass share they represent with respect to the whole system. These quantities are collected and displayed in Fig. 4 as functions of time. The upper left panel shows the total number of subhaloes N_{sat}^{tot} found in the FDM and CDM simulations, as well as the subsample CDM-CUT, identified by solid orange, solid blue, and dashed blue lines, respectively; the lower left panel represents the ratio between FDM and the CDM and CDM-CUT samples. Using the same colour-coding, the right panels display the total subhalo mass contribution M_{sat}^{tot} – i.e. the sum of the mass of all subhaloes – again presented both in absolute values (upper right panel) and relative terms (lower right panel). Poissonian statistical errors are depicted as shaded areas.

In the FDM scenario, there is a great reduction in the total number of subhaloes with respect to CDM, as expected. In this particular system and for the FDM boson mass m_χ under consideration, the ratio is found to be stable in the $0.1 - 0.3$ per cent range. When comparing FDM and CDM-CUT subhaloes belonging to the same mass range, the ratio is two dex larger, approximately $10 - 30$ per cent. These ratios appear to be rather constant throughout the simulation.

The mass share found in subhaloes is reduced as well; however, in this case a trend is noticeable: the total subhalo mass in FDM is approximately ~ 20 per cent the one in CDM around redshift $z \sim 2$, but this difference becomes less pronounced in time, with a value of ~ 60 per cent at redshift $z = 0$. Restricting the analysis on the same mass range, after an initial suppression, FDM approaches CDM-CUT and the two become statistically consistent after $z \sim 0.5$.

The relative number and mass of subhaloes found in FDM and CDM and their evolution are consistent with two specific physical effects introduced by the FDM cosmology. On the one hand, the typical absence of FDM overdensities at small scales at high redshift directly translates in a lower number of substructures that are eventually able to form; on the other hand, as the quantum Jeans scale becomes smaller and smaller, gravity overtakes the repulsive effect of QP and the most massive subhaloes – that dominate the FDM and CDM-CUT samples – are able to non-linearly accrete more and more mass, eventually reaching a similar final mass as their CDM counterparts (see Nori & Baldi 2018).

The impact of such rapid catch-up is even more noticeable in the evolution of the SubHalo Mass Function (SHMF). The SHMF at

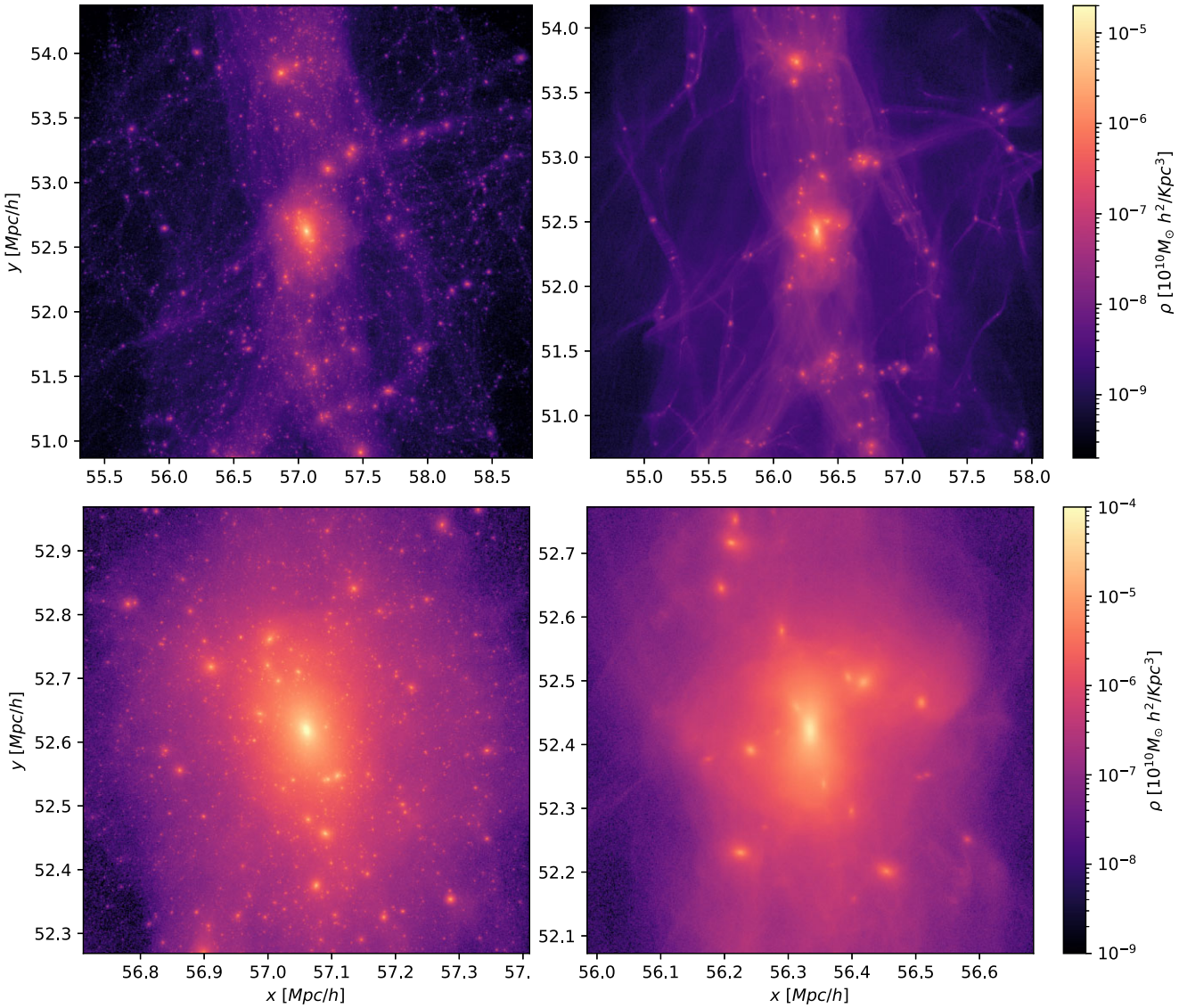

Figure 2. Density maps at $z = 0$ of the CDM (left panels) and FDM (right panels) of the high-resolution region in a 3.5 Mpc/h side cube (top panels) and a zoom of 0.7 Mpc/h side on the main system (bottom panels).

redshift $z = 0$ is displayed in the left panel of Fig. 5 for FDM (orange) and CDM (blue), respectively, with the shaded region representing the Poissonian error associated with the finite number of objects. To better visualize the evolution of the SHMF in time, in the right panel of Fig. 5 the SHMFs are displayed at various redshift using a gradient in the colour shades – ranging from the lightest shade at $z = 4$ to the darkest at redshift $z = 0$. Poissonian error is omitted in this case to improve readability. The mass cut imposed in the FDM case is visualized by a change in colour and linestyle (solid orange to dashed grey).

Comparing the evolution of the SHMFs, it is possible to see that the number of CDM subhaloes grows consistently across all mass bins maintaining the scaling $M_{sat}^{-0.9}$ (one of the main results of the original Aquarius paper, Springel et al. 2008). On the contrary, the number of subhaloes in FDM – starting well below the CDM counterpart due to the power suppression in the initial conditions – evolves unevenly, with the higher mass end growing much faster than the lower end and effectively overlapping with the CDM SHMF at low redshift, due to the gravitational catch-up effect.

To summarize, these results on the number and mass of subhaloes confirm that in FDM the number of subhaloes is reduced, in particular at the expenses of the smallest subhaloes. When considering the most massive subhaloes, the reduction in number and mass share is less pronounced with respect to CDM in the same mass range, altough still observable. Even though these massive subhaloes are the most likely to host an observable bright baryonic counterpart, the considerable departure of the HMFs is very likely to translate in an observable difference in the luminosity function (as shown for other dark matter models as WDM in Macciò & Fontanot 2010). In fact, the number of dark matter subhaloes found for the FDM mass $m_{22} = 2.5\ h$ is lower than the number of luminous Milky-way satellites observed (see data collected in Pace, Erkal & Li 2022, and references therein) and expected by extrapolation (Newton et al. 2018; Nadler et al. 2020).

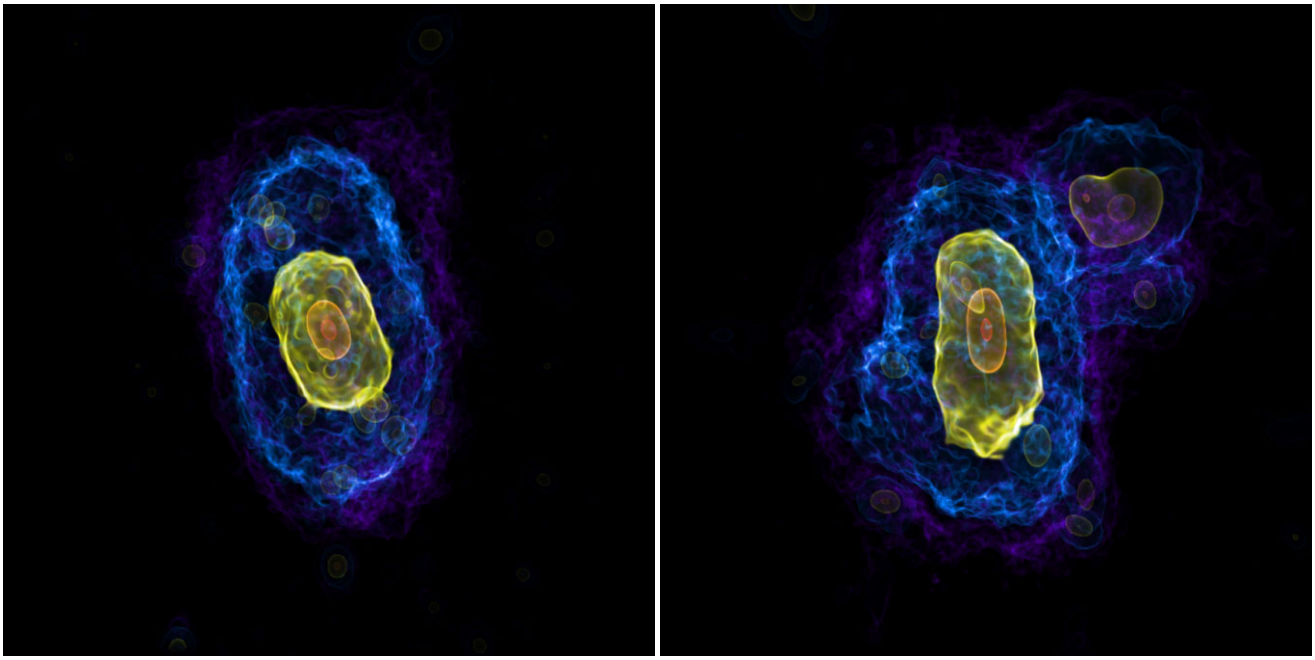

Figure 3. Density renderings of the main halo in the CDM (left) and FDM (right) scenario. Colours represent iso-density surfaces at different density values within a box of 1 Mpc/h. A movie of the 360° rotation around the y-axis can be found in the online supplement material.

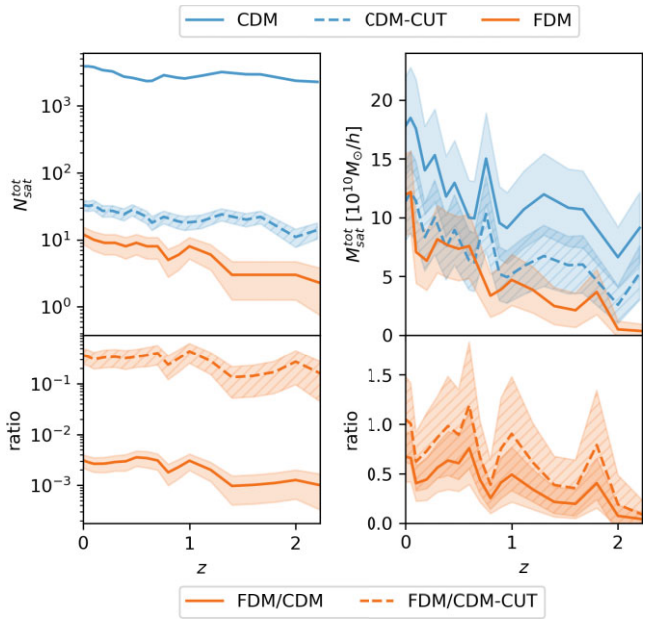

Figure 4. Evolution of the total number of subhaloes (left panels) and their total mass (right panels) in time. The results obtained for the CDM (solid blue), the CDM-CUT (dashed blue), and the FDM (solid orange) samples are displayed in absolute terms in the top panels. Bottom panels show the ratio of the quantities above (solid and dashed lines for the FDM/CDM and FDM/CDM-CUT, respectively). 1σ statistical errors are included as shaded regions.

4.1.2 Distance and velocity distribution

The different dynamics introduced in the FDM scenario has an impact not only on the number and mass of subhaloes, as we detailed in the previous subsection, but also on the overall properties of subhaloes in terms of position and velocity.

The pair-wise distributions of distance, velocity, and mass are displayed in Fig. 6 where points in the parameter spaces represent subhaloes found at redshift $z < 1$. Integrated distributions in mass are collected in the right panels (the stacking on redshift is meant to avoid a low-count statistics in the FDM case). The FDM (orange) and CDM (blue) points at various redshifts are once again depicted using a gradient in the colour shading.

The vertical dashed line in the left panels represents the mass cut M_{CUT} applied to the FDM and CDM-CUT samples. For comparison, the integrated distributions – each depicted with its own shaded 1σ confidence region – are plotted alongside the integrated distribution of the CDM-CUT subsample that satisfy $M_{sat} > M_{CUT}$ (dashed blue line).

In the FDM scenario, subhaloes can be found at larger distances with respect to CDM-CUT, with a statistical shift of ∼50 kpc/h separating the peak of the two distributions obtained in the same mass range (note also that the peak of the CDM-CUT distribution itself is ∼50 kpc/h shifted farther away from the centre with respect to the total CDM one). Other than the peak itself, the difference in the distributions seems to be more prominent in the tails: FDM subhaloes are statistically found at larger distances than CDM and are scarse in the vicinity of the centre of the system. The velocity distributions are statistically consistent with each other, with a small preference for low velocity in FDM with respect to the CDM case, although not dramatically significant.

Ultimately, the combined analysis of these distributions confirms that subhaloes in FDM are statistically found at a larger distance from the centre and do not reach the high velocities observed in CDM. This is due to the lack of low-mass subhaloes that in CDM case contribute to the high velocity and to small distance tails of the two distributions. Low-mass subhaloes in FDM are in general less numerous than the ones in CDM as small overdensities are not present in the initial conditions. However, the few low-mass subhaloes that are indeed able to form in FDM are found

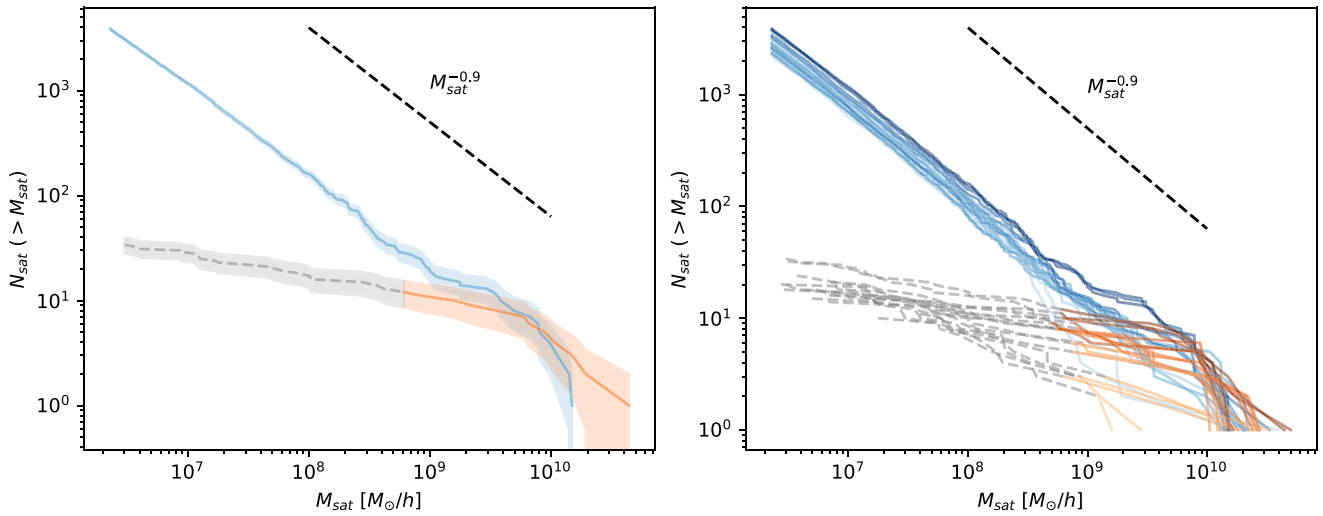

Figure 5. SHMF of the CDM (blue) and FDM (orange) systems, at redshift $z = 0$ (left) and at multiple redshifts (right). In the latter, different redshift from $z = 4$ and $z = 0$ are identified by a gradient in the colour shade, from lightest to darkest. In the left panel, we also show the Poissonian error (shaded region), not present in the right panel for readability purposes. The FDM SHMF is represented by a grey dashed line for masses below the mass cut M_{CUT}.

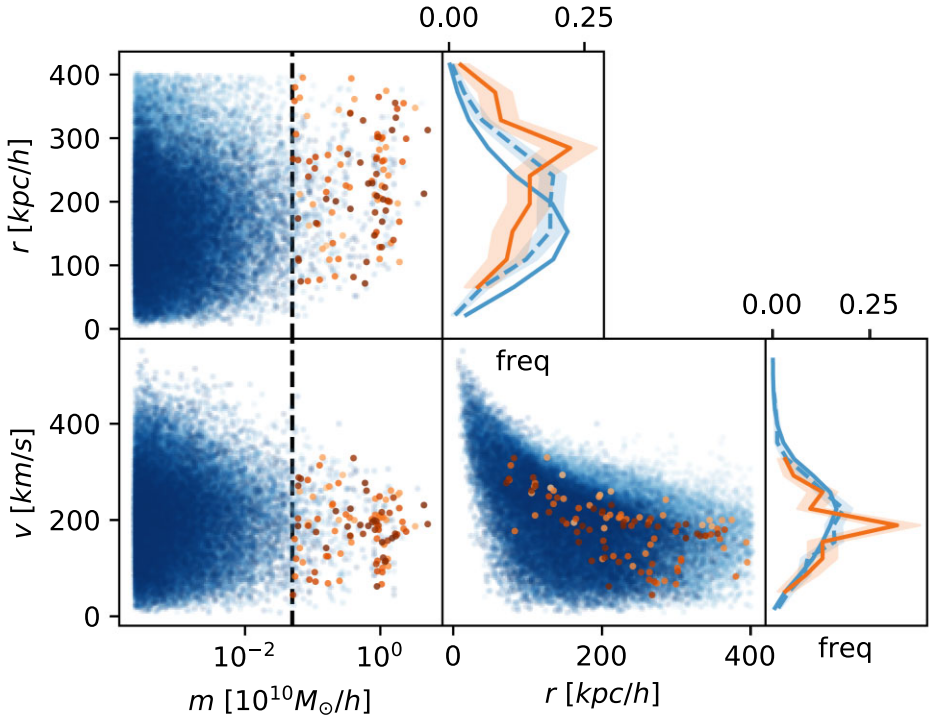

Figure 6. Distributions of subhalo properties in terms of distance, velocity, and mass in the FDM (orange) and CDM (blue) simulations. The vertical dashed line in left panels represents the mass cut M_{CUT}. Integrated distributions of subhaloes in distance and velocity in the two simulations are featured on the right side each with its own shaded 1σ confidence region, where the distribution of CDM subhaloes with $M_{sat} > M_{CUT}$ is added for comparison (dashed blue). To avoid a very low count statistics in the FDM case, subhaloes in snapshots at redshift $z < 1$ are here stacked together.

statistically farther away from the halo and have a lower velocity. This is a strong indication that the properties of subhaloes are also affected by dynamic processes in the evolution of the system, most possibly through an enhanced stripping effect exerted by the halo on small and close subhaloes in the FDM cosmology. For example, enhanced stripping rates have been found in simulations of WDM models, that like FDM ones reduce the concentration of dark matter subhaloes (Lovell et al. 2021). Moreover, we acknowledge that numerical investigations suggest that haloes in *N*-body simulations can be stripped or even disrupted by resolution effects (e.g. van den Bosch & Ogiya 2018; Errani & Navarro 2021), even though the selection related to numerical fragmentation should in principle discard the majority of subhaloes where resolution effects are most prominent. Ultimately, full hydro simulations will be needed to probe the effects of the different dynamical evolution of the stellar content in subhaloes, since dark matter and stars react differently to stellar

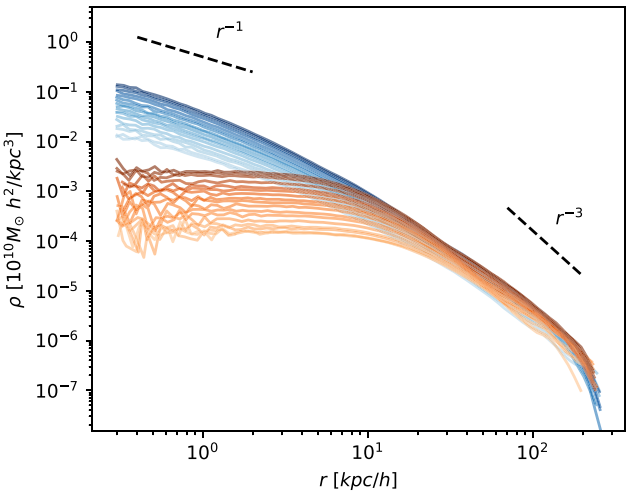

Figure 7. Radial dark matter density profiles of the MW-analogue halo in FDM (orange) and CDM (blue). Profiles at different redshifts are displayed with a gradient in shading, as in Fig. 5.

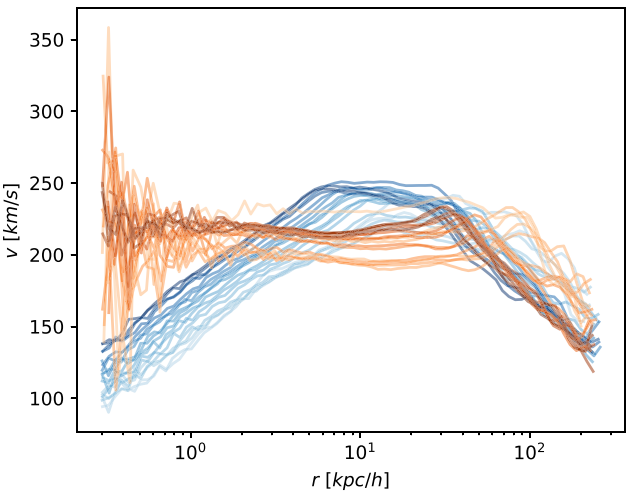

Figure 8. Radial dark matter velocity profiles of the MW-analogue halo in FDM (orange) and CDM (blue). Profiles at different redshifts are displayed with a gradient in shading, as in Fig. 5.

stripping (Peñarrubia, Navarro & McConnachie 2008; Macciò et al. 2021).

4.1.3 Properties of the halo

Let us now focus on the properties of the halo. Given its high mass and large size, its global properties are less affected by the additional physics of FDM – that has only an impact on the inner region – with respect to subhaloes. In fact, the total mass of the halo in the FDM and CDM scenarios are comparable at all redshifts within a ± 20 per cent range, with the largest deviations coming from different timings in the major merger events. Nevertheless, a deviation in the radial profiles induced by the typical repulsive FDM interaction is indeed expected.

In Fig. 7, the radial density profile of the Milky-way-like analogue is displayed both for the FDM (orange) and CDM models (blue). The lower and upper radial limits are 3.5 kpc/h (i.e. approximately 3 times the softening length ϵ) and the virial radius, respectively. For the two scenarios, profiles at multiple redshifts are displayed with a shade gradient – i.e. going from lighter to darker shades from $z = 2.5$ to $z = 0$ – to visually represent the evolution of the profile in time.

As clearly visible, while the CDM profile is consistent with an NFW profile, the FDM one features the typical combination of a core in the centre and an NFW tail. This comes as no surprise, as it is known that the stable configuration of FDM haloes is indeed characterized by a core sustained by the repulsive effect of the QP, as described in Section 2.2. As an additional check on the accuracy of the profiles, we calculated the Power radius (Power et al. 2003) at $z = 0$ for the FDM case and compared it to the CDM one (as done in Springel et al. 2008, Section 2.4). The radius found is $\sim$0.8 kpc/h, which is approximately 1.8 times its CDM counterpart due to the different number of particles in the central region: this is one order of magnitude lower than the size of the FDM core $R_c = 8.47$ kpc/h and thus it does not affect the results discussed in the following.

In this cored configuration, the phase of the wave-function – related to the fluid velocity in the Madelung formulation – is position independent; thus, a core in the density distribution is paired with a *plateau* in the velocity distribution (Hui et al. 2017). Heuristically, as the FDM core is defined as the solution for which the gravitational self-attraction is compensated by an opposite force at all points, no velocity gradient is needed for the core self-sustainment, contrary to the CDM case. To highlight this peculiar effect, the velocity radial profiles are shown in Fig. 8 for the halo in the CDM (blue) and FDM (orange) scenarios, with the same radial limits and shade gradient to represent different redshift as in Fig. 7.

Regarding the CDM model, the velocity profile is consistent with an NFW density profile. In fact, in CDM we can use the following qualitative estimate: assuming virialization, the velocity profile $v(r)$ given by a power-law density distribution $\rho(r) \sim r^{-n}$ is related to the mass $M(r)$ enclosed within r as $v(r) \sim \sqrt{M(r)/r}$, thus $v(r) \sim r^{-n/2+1}$. Since the NFW density profile is characterized by a double power-law behaviour with inner $\rho(r) \sim r^{-1}$ and outer $\rho(r) \sim r^{-3}$ scalings, the velocity profile observed $v(r) \sim r^{+1/2}$ and $v(r) \sim r^{-1/2}$ are indeed consistent with predictions.

In FDM, instead, it is not possible to invoke the same simple estimate as the scaling $v(r) \sim \sqrt{M(r)/r}$ is obtained by assuming equilibrium between the kinetic and gravitational energy only, while the quantum energy typical of FDM should be included in this case. In the outskirts of the halo of the NFW-like tail, the velocity profiles of FDM and CDM are consistent with each other as the quantum energy contribution is negligible in the integration – being dominant only in the innermost region – while inside the core the different dynamics translates in a velocity *plateau*, as previously discussed.

While the inner cored feature in the dark matter density profile can be reproduced dynamically by many dark matter scenarios alternative to CDM, this very interesting feature in the velocity profile is directly linked to the presence of an additional interaction that FDM has in common with other dark matter models – as e.g. Self-interacting Dark Matter models (Robertson et al. 2019) – and sets FDM apart from models that produce density cores without self-interaction – as e.g. thermal WDM. Indeed, even though it may be hard to observe, this is a clean feature to discriminate CDM and non self-interacting dark matter models as WDM from FDM. Of course, given that this work is restricted to a dark-matter-only scenario, this peculiar feature might be potentially observable in astrophysical systems where the baryonic content is negligible, as dwarf galaxies or smaller systems.

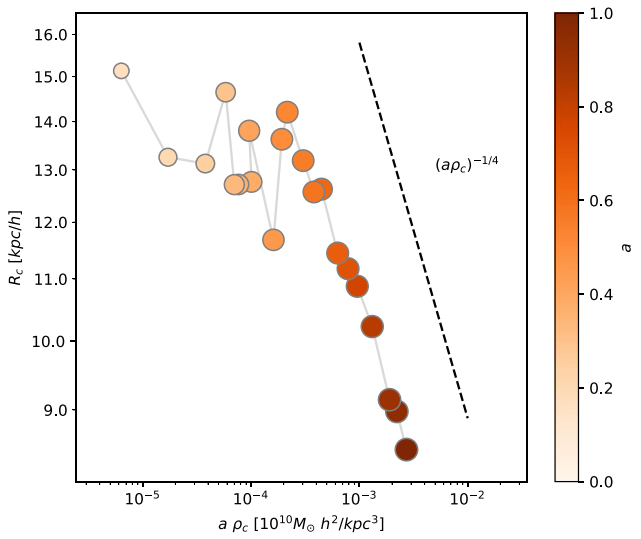

Figure 9. Evolution of the core properties in the (ρ_c, R_c) parameter space. The scaling $R_c \sim (a\rho_c)^{-1/4}$ is here given as a reference for the slope with no particular normalization.

4.2 Specific FDM core properties

In the previous section, we verified that the halo hosts an FDM core associated with a velocity plateau, identifying the solution of the spherical mEP system of equation (8). In this section, we now tackle the specific properties of the core in more detail, including the subhaloes in this analysis.

Before presenting the results, let us first recall our expectations about the solitonic state of an FDM core. In a purely ideal and isolated case, a spherically symmetric core solution in an excited state should eventually relax and reach the solitonic state – i.e. the ground state of the system – exhibiting a purely quantum transition between discreet excitation levels associated with sudden energetic emissions. Of course, the discreet nature of this quantum process is less dramatic when considering a not-idealized and rather chaotic physical system such as the formation of dark matter structures, with a large number of degrees of freedom – e.g. intrinsic and collective motion, morphological asymmetry, etc. – so that excited systems are able to slowly dissipate energy and their relaxation process to reach the ground state is rather smooth.

It is thus reasonable to imagine that the inner cored structure forms in the early stages of the overall system collapse as a result of the competing gravitational and quantum potentials, yet not necessarily in its energetic ground state. In time, with the system relaxation and assuming no external energy input, the core may eventually dissipate its excess energy and gradually reach its solitonic state.

Having this in mind, let us focus on the trajectory of the core of halo in the (ρ, R_c) parameter space, represented in Fig. 9. Here, only the direct progenitor line is considered, meaning that no secondary progenitor branchings are depicted. The position of the core properties in this parameter space is once again displayed for several redshifts from $z = 4$ to $z = 0$ using a shade gradient from lightest to darkest.

It is possible to see that evolution of the halo core properties in time is characterized by an initial *stalling* phase (roughly from $z = 4$ to $z = 1$ in this case) when the density increase is accompanied by only a marginal decrease in radius. After that, the radius decreases more rapidly and the typical scaling $R_c \sim (a\rho_c)^{-1/4}$ – presented in the plot as a dashed line with no particular normalization – is reached and maintained until the end of the simulation.

As another important result of this work, we observe that the process for the core to reach a stable scaling does not seem to be necessarily instantaneous. Of course, the following question naturally arises: are there processes that are able to delay the onset and the eventual stabilization of the expected core scaling?

To tackle this question, let us broaden the sample under consideration and include the subhaloes in this analysis. All 34 subhaloes in our simulations feature an FDM core and serve as valid solutions of the mEP system. Using the conservative cuts $M_{CUT} = 5 \times 10^8 M_\odot/h$ and $s_{CUT} = 0.16$ to account for numerical fragmentation, we restrict our analysis on 12 out of the 34 subhaloes belonging to the system at redshift $z = 0$, noting that the remaining 22 represent < 3 per cent of the total mass found in subhaloes at that redshift. In the following, we are going to study the halo and subhalo cores as part of a single sample, not taking into consideration the great difference in age and environment within which these objects have evolved. We acknowledge that this might be a very important factor, but this is something that only a broader study encompassing a large sample of complex systems (with data on subhaloes) can address, thus falling beyond the scope of this work.

In Fig. 10, the position in the (ρ_c, R_c) parameter space of the halo and the selected subhaloes are displayed, including the secondary progenitor branches recovered from the merger tree analysis (progenitors and descendants in the figure are linked by faint grey lines). As reference, the $R_c \sim (a\rho_c)^{-1/4}$ scalings with the normalization of Schive et al. (2014) (dotted line) and Nori & Baldi (2020)[1] (dot-dashed line) are plotted.

The point size is related to the halo mass, while colour is representative of a different observable for each panel: these represent the scale factor a in the top panel and the fraction of mass accreted via merger from the previous snapshot $M_{\rm merged}/M$ in the bottom one, with $M_{\rm merged}$ as defined in Section 3.2.

Regarding the distribution of the core properties in the parameter space and its relation with redshift (first panel of Fig. 10), it is possible to notice that trajectories are characterized by four overall features:

(i) all cores eventually reach the expected $R_c \sim (a\rho_c)^{-1/4}$ scaling in terms of slope;
(ii) the normalization factor of the final scaling relation is not the same for every core, seemingly showing a positive correlation with the system mass and/or age;
(iii) cores of similar mass and forming at similar redshift seem to share similar trajectories;
(iv) in few cases, trajectories exhibit sudden and abrupt deviations, especially at the nodes of merger tree.

The results in Fig. 10 suggest that all cores end up following the $R_c \sim (a\rho_c)^{-1/4}$ scaling at lower redshifts. In terms of normalization, more massive subhaloes tend to follow a scaling with a higher normalization than the less massive ones, with a factor $\sim$5 of difference over almost four orders of magnitude in mass. This higher normalization factor is also coupled with a more pronounced initial phase of marginal radius decrease (as noted in the halo). More massive subhaloes that formed at a higher redshift thus take statistically more time to reach their final scaling with respect to low mass (and low redshift) ones.

Interestingly, the subhaloes in the same mass range of Nori & Baldi (2020) are consistent with the scaling found in that work,

[1] Specifically $\kappa_{1/4}$ from Table 4 (Nori & Baldi 2020).

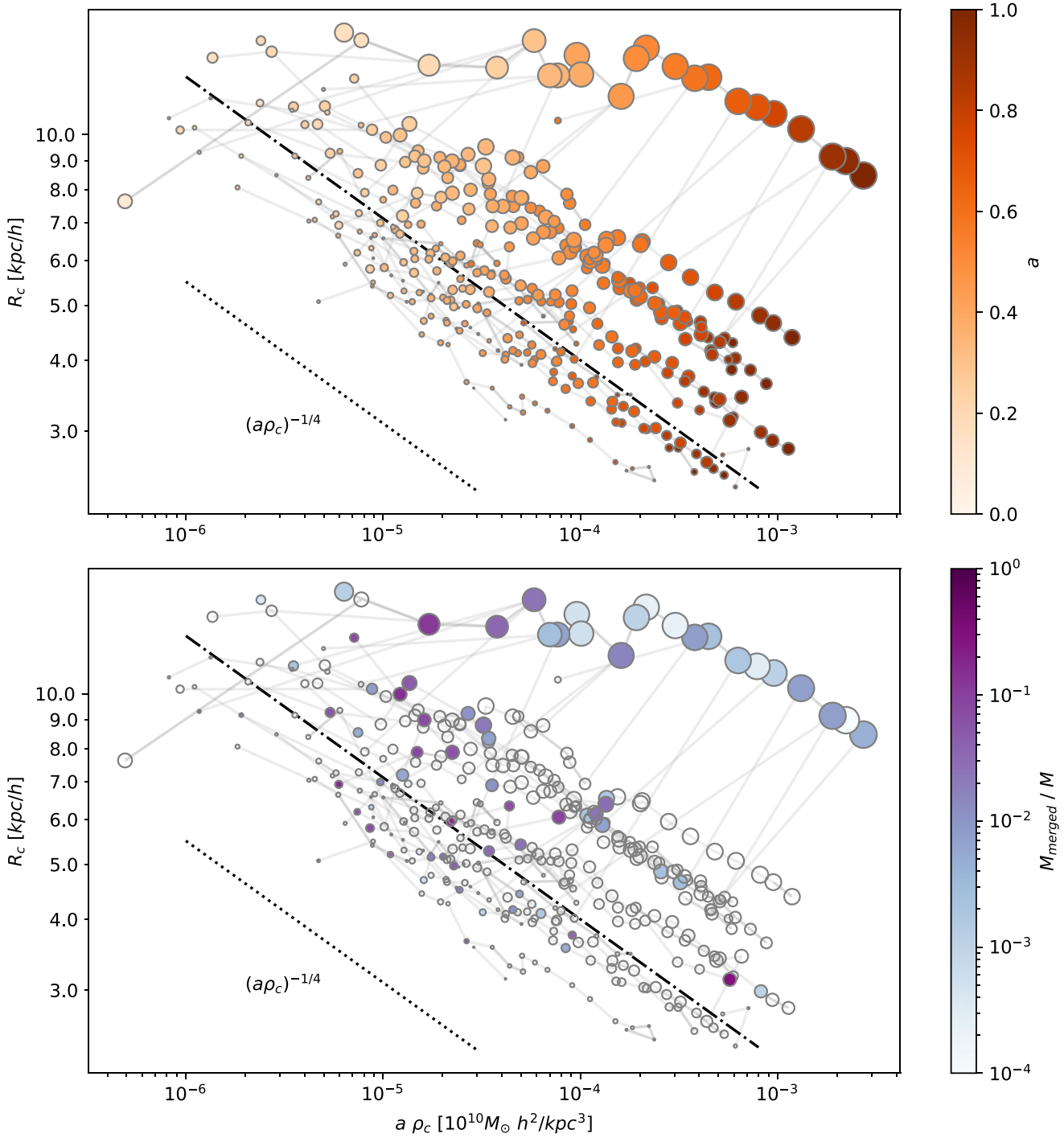

Figure 10. Evolution of the core properties in the (ρ_c, R_c) parameter space space. Point size is related to mass, while the colour represent a different observable for each panel; these are the scale factor a (top panel) and the fraction of mass accreted via merger $M_{\rm merged}/M$ from the previous redshift (bottom panel). The black lines represent the typical $R_c \sim (a\rho_c)^{-1/4}$ scaling with Schive et al. (2014) (dotted) and Nori & Baldi (2020) (dotted dashed) normalization.

proving the consistency of the results of different systems and different resolutions. In Nori & Baldi (2020), this scaling was studied considering a collection of zoom-in systems with different masses across two orders of magnitude, finding that the overall scaling relation was generally tilted and influenced by the state of relaxation of the systems. Given the results obtained in this work, we can conclude that the tilt in the overall scaling relation observed in Nori & Baldi (2020) originated from calculating a single slope using systems that reached the same scaling relation but at different times and with different normalizations (it is possible indeed to recognize *a posteriori* this effect in the left panels of Fig. 6 in Nori & Baldi (2020)).

The sudden deviation that some trajectories exhibit are preferentially found at merger events – highlighted in the bottom panel.

Indeed, it would be reasonable to claim that merger events might play an important role in delaying the realization of the scaling and even temporarily disrupting it. The amount of mass accreted via merger also appears to be more relevant in the initial *stalling* phase, supporting a potential role in this sense.

However, it is important to stress that the hierarchical formation of structures – that holds also in FDM cosmologies – comes with an intrinsic positive correlation between the mass of objects, their age, and the number/importance of merger events they experienced, so it impossible at this stage to conclude which one of these properties has a direct causal effect on the normalization of the FDM scaling. Moreover, even if this correlation is physically reasonable and seems to be consistently present in simulations of different systems and resolutions, it is impossible to exclude – as well as to confirm – a possible numerical origin, mainly related to the SPH nature of the algorithm. This, in fact, could be only tested in a direct comparison between simulations of the same system with a particle-based and a grid-based approach, which still is somehow difficult to design due to the different numerical limits on scale and resolution that the two methods have.

5 CONCLUSIONS

In this work, we presented a high-resolution simulation of the formation and evolution of a Milky-way-like halo extracted from the Aquarius project in the framework of FDM cosmologies. With the use of the *N*-body code AX-GADGET, we were able to simulate such a complex system, with a massive central object and a considerable population of subhaloes, without neglecting the typical quantum interaction of FDM.

We first detailed the global properties of subhaloes, presenting – for the first time in the literature – a self-consistent SHMF in an FDM system. In the comparison with its CDM counterpart, the overall number of subhaloes is greatly reduced, especially for the least massive ones. The total mass found in subhaloes is reduced as well. In terms of distance and velocity, subhaloes in FDM are statistically found at larger distances and have lower speed.

With the FDM mass $m_\chi = 2.5h \times 10^{-22}\,\mathrm{eV}/c^2$ adopted in this work – chosen to highlight the effect of FDM dynamics on galaxy formation processes as a proof of concept – the number of dark matter subhaloes in FDM is well below the number of luminous satellites observed (see data collected in Pace et al. 2022, and references therein) and expected by extrapolation (Newton et al. 2018; Nadler et al. 2020). Of course, a larger value of the FDM mass would enhance the number of dark matter subhaloes, thus representing a viable model in terms of number of luminous counterparts.

The halo exhibits the typical cored structure of FDM in the radial density profile. Its dark matter radial velocity profile is characterized by a flattening in the core region: this feature, that to our knowledge is observed in this work for the first time for FDM, is indeed a specific feature of FDM that sets the model apart from other non self-interacting dark matter models such as WDM, although being hardly observable at the moment.

Studying the evolution of the radius and density of this core, we observe that the theoretical scaling relation $R_c \sim (a\rho_c)^{-1/4}$ is asymptotically approached, after an initial stalling phase where the radius only marginally decreases.

Finally, the evolution of the core properties of the halo was framed in a broader context by studying the combination of the core in the halo as well as the cores of subhaloes. The properties of all cores satisfy the scaling relations, although the specific normalization was unexpectedly found to mildly correlate with the system mass – or equivalently with age or merger events, as these properties are all related to each other.

This work shows that the properties of cores that theoretically follow rather simple FDM scaling relations exhibit a more complex behaviour, characterized in some cases by a delayed establishment of the scaling relation (and not immediate from formation onwards). Such scaling is also not necessarily universal in terms of normalization, when systems across multiple orders of magnitude in mass are considered. The interplay between subsystems and the peculiar history of each subsystem can indeed play a role in such differentiation. These effects seem to be more pronounced for the most massive systems in our analysis, thus suggesting that the indiscriminate use of the scaling relations to confirm or rule out FDM models in comparison with observations might be incorrect when the extrapolation extends indefinitely over various orders of magnitude in mass.

ACKNOWLEDGEMENTS

The authors thank Prof. Adrian Jenkins, who provided the original Aquarius CDM simulation and helped the authors in the realization of the initial conditions for FDM. This material is based upon work supported by Tamkeen under the New York University Abu Dhabi Research Institute grant CAP3. MB acknowledges support by the project 'Combining Cosmic Microwave Background and Large Scale Structure data: an Integrated Approach for Addressing Fundamental Questions in Cosmology', funded by the MIUR Progetti di Ricerca di Rilevante Interesse Nazionale (PRIN) Bando 2017 – grant 2017YJYZAH. The authors gratefully acknowledge the High Performance Computing resources at New York University Abu Dhabi and at the parallel computing cluster of the Open Physics Hub (https://site.unibo.it/openphysicshub/en) at the Physics and Astronomy Department in Bologna.

DATA AVAILABILITY

The data underlying this article will be shared on reasonable request to the corresponding author.

REFERENCES

Albert A. et al., 2017, ApJ, 834, 110
Alcock C. et al., 1993, Nature, 365, 621
Armengaud E., Palanque-Delabrouille N., Marsh D. J. E., Baur J., Yèche C., 2017, MNRAS, 471, 4606
Arvanitaki A., Geraci A. A., 2014, Phys. Rev. Lett., 113, 161801
Banerjee A., Budker D., Eby J., Flambaum V. V., Kim H., Matsedonskyi O., Perez G., 2020, Journal of High Energy Physics, 2020
Bennett C., et al., 2013, ApJS, 208, 20
Bertone G., Hooper D., Silk J., 2005, Phys. Rept., 405, 279
Bode P., Ostriker J. P., Turok N., 2001, ApJ, 556, 93
Bohm D., 1952, Phys. Rev., 85, 166
Braine T. et al., 2020, Phys. Rev. Lett., 124, 101303
Buonaura A., 2018, PoS, DIS2017, 079
Chan H. Y. J., Ferreira E. G. M., May S., Hayashi K., Chiba M., 2022, MNRAS, 511, 943
Chavanis P.-H., 2011, Phys. Rev. D, 84, 043531
Chavanis P. H., 2012, A&A, 537, A127
Chavanis P.-H., Delfini L., 2011, Phys. Rev. D, 84, 043532
Danninger M., 2017, J. Phys. Conf. Ser., 888, 012039
Davis M., Efstathiou G., Frenk C. S., White S. D., 1985, Astrophys.J., 292, 371
Du X., Behrens C., Niemeyer J. C., Schwabe B., 2017, Phys. Rev., D95, 043519

Errani R., Navarro J. F., 2021, MNRAS, 505, 18
Feng J. L., 2010, Ann. Rev. Astron. Astrophys., 48, 495
Ferreira E. G. M., 2021, Astron. Astrophys. Rev., 29
Graham P. W., Rajendran S., 2013, Phys. Rev. D, 88, 035023
Gross E. P., 1961, Il Nuovo Cimento, 20, 454
Hlozek R., Grin D., Marsh D. J. E., Ferreira P. G., 2015, Phys. Rev., D91, 103512
Hu W., Barkana R., Gruzinov A., 2000, Phys. Rev. Lett., 85, 1158
Hui L., Ostriker J. P., Tremaine S., Witten E., 2017, Phys. Rev., D95, 043541
Iršič V., Viel M., Haehnelt M. G., Bolton J. S., Becker G. D., 2017, Phys. Rev. Lett., 119, 031302
Ji S. U., Sin S. J., 1994, Phys. Rev., D50, 3655
Jungman G., Kamionkowski M., Griest K., 1996, Phys. Rept., 267, 195
Kamionkowski M., 1998, in E. Gava, A. Masiero, Narain K. S., Randjbar-Daemi S., Senjanovic G., Smirnov A., Shafi Q., Proc. ICTP Summer School in High-Energy Physics and Cosmology, Vol. 14. WIMP and Axion Dark Matter. World Scientific Publishers, Singapore, p. 394
Katz N., Quinn T., Bertschinger E., Gelb J. M., 1994, MNRAS, 270, L71
Klypin A. A., Kravtsov A. V., Valenzuela O., Prada F., 1999, ApJ, 522, 82
Kolb E. W., Tkachev I. I., 1993, Phys. Rev. Lett., 71, 3051
Kolb E. W., Tkachev I. I., 1994, Phys. Rev. D, 49, 5040
Lovell M. R., Frenk C. S., Eke V. R., Jenkins A., Gao L., Theuns T., 2014, MNRAS, 439, 300
Lovell M. R., Cautun M., Frenk C. S., Hellwing W. A., Newton O., 2021, MNRAS, 507, 4826
Macciò A. V., Fontanot F., 2010, MNRAS: Lett, 404, L16
Macciò A. V., Prats D. H., Dixon K. L., Buck T., Waterval S., Arora N., Courteau S., Kang X., 2021, MNRAS, 501, 693
Madelung E., 1927, Zeitschrift für Physik, 40, 322
Majorovits B., et al., 2020, J. Phys. Conf. Ser., 1342, 012098
Marsh D. J. E., 2016, Phys. Rept., 643, 1
May S., Springel V., 2021, MNRAS, 506, 2603
McAllister B. T., Flower G., Ivanov E. N., Goryachev M., Bourhill J., Tobar M. E., 2017, Phys. Dark Univ., 18, 67
Milgrom M., 1983, ApJ, 270, 365
Mocz P., Vogelsberger M., Robles V. H., Zavala J., Boylan-Kolchin M., Fialkov A., Hernquist L., 2017, MNRAS, 471, 4559
Nadler E. O. et al., 2020, ApJ, 893, 48
Navarro J. F., White S. D. M., 1994, MNRAS, 267, 401
Newton O., Cautun M., Jenkins A., Frenk C. S., Helly J. C., 2018, MNRAS, 479, 2853
Nori M., Baldi M., 2018, MNRAS, 478, 3935
Nori M., Baldi M., 2020, MNRAS, 501, 1539
Nori M., Murgia R., Iršič V., Baldi M., Viel M., 2019, MNRAS, 482, 3227
Oh S.-H., de Blok W. J. G., Brinks E., Walter F., Kennicutt R. C. Jr, 2011, Astron. J., 141, 193
Ouellet J. L., et al., 2019, Phys. Rev. D, 99, 052012
Pace A. B., Erkal D., Li T. S., 2022, ApJ, 940, 136
Peccei R. D., Quinn H. R., 1977a, Phys. Rev. D, 16, 1791
Peccei R. D., Quinn H. R., 1977b, Phys. Rev. Lett., 38, 1440
Peebles P. J. E., 1980, The Large-Scale Structure of the Universe. Princeton University Press, Princeton, NJ
Peñarrubia J., Navarro J. F., McConnachie A. W., 2008, ApJ, 673, 226
Pitaevskii L. P., 1961, Sov. Phys. JETP, 13, 451
Planck Collaboration XIII, 2016, A&A, 594, A13
Power C., Navarro J. F., Jenkins A., Frenk C. S., White S. D. M., Springel V., Stadel J., Quinn T., 2003, MNRAS, 338, 14
Robertson A., Harvey D., Massey R., Eke V., McCarthy I. G., Jauzac M., Li B., Schaye J., 2019, MNRAS, 488, 3646
Schive H.-Y., Tsai Y.-C., Chiueh T., 2010, ApJS, 186, 457
Schive H.-Y., Chiueh T., Broadhurst T., 2014, Nature Phys., 10, 496
Schive H.-Y., Chiueh T., Broadhurst T., Huang K.-W., 2016, ApJ, 818, 89
Schive H.-Y., ZuHone J. A., Goldbaum N. J., Turk M. J., Gaspari M., Cheng C.-Y., 2018, MNRAS, 481, 4815
Schneider A., Smith R. E., Maccio A. V., Moore B., 2012, MNRAS, 424, 684
Schwabe B., Niemeyer J. C., Engels J. F., 2016, Phys. Rev., D94, 043513
Sikivie P., 2008, Lect. Notes Phys., 741, 19
Springel V. et al., 2008, MNRAS, 391, 1685
Tollet E., et al., 2016, MNRAS, 456, 3542
van den Bosch F. C., Ogiya G., 2018, MNRAS, 475, 4066
Veltmaat J., Niemeyer J. C., Schwabe B., 2018, Phys. Rev., D98, 043509
Viel M., Lesgourgues J., Haehnelt M. G., Matarrese S., Riotto A., 2005, Phys. Rev., D71, 063534
Wang J., White S. D. M., 2007, MNRAS, 380, 93
Woo T.-P., Chiueh T., 2009, AJ, 697, 850

SUPPORTING INFORMATION

Supplementary data are available at *MNRAS* online.

suppl_data

Please note: Oxford University Press is not responsible for the content or functionality of any supporting materials supplied by the authors. Any queries (other than missing material) should be directed to the corresponding author for the article.

This paper has been typeset from a TEX/LATEX file prepared by the author.